A Low-Subharmonic, Full-Range, and Rapid Pulse Density Modulation Strategy for ZVS Full-Bridge Converters

Hongchang Li, *Member, IEEE*, Shuxin Chen, *Student Member, IEEE*, Jingyang Fang, *Student Member, IEEE*, Yi Tang, *Senior Member, IEEE*, and Michael A. de Rooij, *Senior Member, IEEE*

***Abstract*—The pulse-density-modulation (PDM) zero-voltage-switching (ZVS) full-bridge converter is a promising power converter for wireless power transfer (WPT) systems. The converter has the advantages of both direct conversion ratio control and load-independent soft switching. These advantages reduce the overall system complexity and power loss. However, the converter suffers from the limitations of large low-frequency subharmonics, a narrowed modulation range, and a large modulation delay. These limitations are caused by the existing PDM strategy, which was designed to generate a symmetric ZVS current to ensure the ideal ZVS for minimizing the switching loss. This paper finds that even with an asymmetric ZVS current, the ideal ZVS can still be ensured by the negative feedback effect of the dead-time voltage. Based on this finding, a PDM strategy that allows asymmetric ZVS currents is proposed to overcome the aforementioned limitations. In experiments, a ZVS full-bridge converter was modulated by the existing and the proposed PDM strategies, respectively. The converter performances and responses were compared and the results showed that the proposed PDM strategy can overcome the limitations while achieving ZVS. The proposed PDM strategy was also tested in a WPT system for verification.**

***Index Terms*—Dead-Time, pulse-density-modulation (PDM), wireless power transfer (WPT), zero-voltage-switching (ZVS).**

NOMENCLATURE

V_{dc}	Converter dc side voltage [V].
d	Pulse density.
f_s	Fundamental switching frequency [Hz].
T_s	Fundamental switching period [s].
T_{dead}	Dead-Time period [s].
C_{OSSQ}	Charge equivalent switch output capacitance [F].

Manuscript received October 20, 2018; accepted December 17, 2018. Date of publication December 24, 2018; date of current version June 10, 2019. This work was supported by Nanyang Technological University under Grant NTU-SUG M4081608. Recommended for publication by Associate Editor O. C. Onar. *(Corresponding author: Yi Tang.)*

H. Li is with the Energy Research Institute, Nanyang Technological University, Singapore 639798 (e-mail:

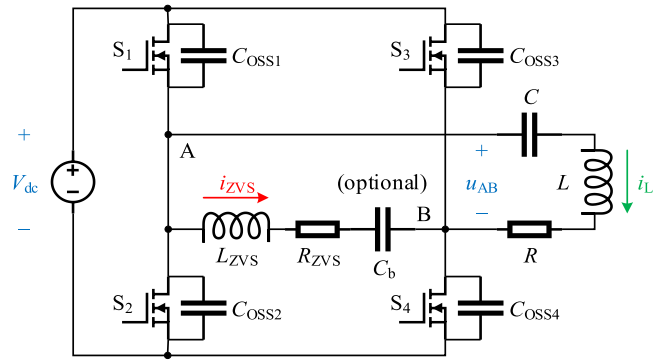

Fig. 1. Circuit diagram of PDM ZVS full-bridge converter [18].

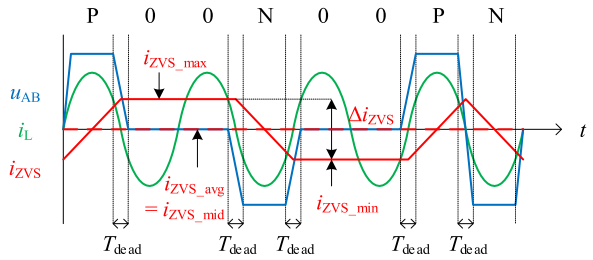

Fig. 2. Ideal operating waveforms with the existing PDM strategy [18].

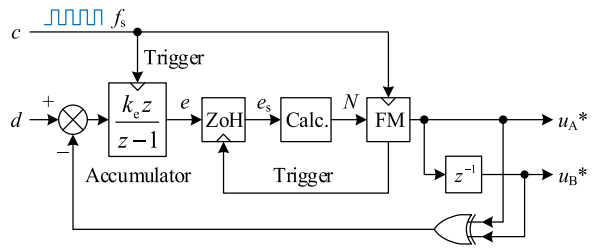

Fig. 3. Block diagram of the existing PDM strategy [18].

switching. The equivalent series resistance (ESR) of the ZVS branch is denoted by R_{ZVS}.

The waveforms shown in Fig. 2 were derived from the existing PDM strategy [18], whose block diagram is shown in Fig. 3. The strategy was elaborately designed to generate a symmetric i_{ZVS} to ensure the ideal ZVS for minimizing the switching loss. However, the converter with the existing PDM strategy suffers from the limitations of large low-frequency subharmonics on u_{AB}, a narrowed modulation range, and a large modulation delay. The large low-frequency subharmonics are created by the nested frequency modulator "FM" and lead to large ripples on the converter input and output power. The modulation range is narrowed by the lower limit on the pulse density d. The limit is to prevent "FM" from falling into a too long modulation period but it reduces the range of conversion ratio. The large modulation delay is introduced by the small accumulation coefficient k_e that ensures the stability of the delta-sigma loop [18].

This paper finds that even with an asymmetric i_{ZVS}, the ideal ZVS can still be ensured if C_b is removed, as the experimental waveforms shown in Fig. 4, where the asymmetric i_{ZVS} has a nonzero average (−0.5 A) and a near-zero midrange, and the

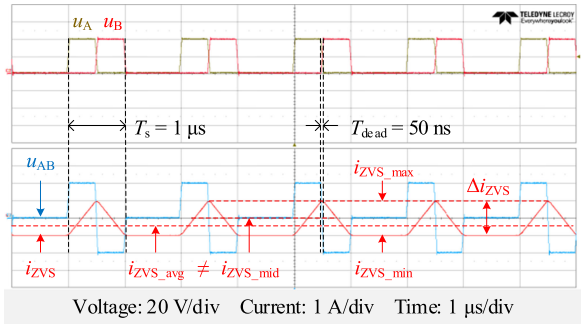

Fig. 4. ZVS achieved with an asymmetric ZVS current.

absolute values of the minimum and maximum i_{ZVS} both equal the optimal current (1 A) for ideal ZVS. The mechanism is explained in Section II by the negative feedback effect of the dead-time voltage. By using this effect, Section III proposes a simplified PDM strategy that allows asymmetric i_{ZVS} and overcomes the limitations of the existing PDM strategy. Experiments of a standalone converter and a WPT system are given in Sections IV and V, respectively. Section VI concludes the paper.

II. Negative Feedback Effect of Dead-Time Voltage

A. Dead-Time Transients and Switching Modes

As shown in Figs. 2 and 4, a PDM ZVS full-bridge converter may have six types of dead-time transients when u_{AB} changes between the positive (P), negative (N), and zero (0) states. In Fig. 5, the six types of transients are denoted by 1) N-to-0, 2) 0-to-P, 3) N-to-P, 4) P-to-0, 5) 0-to-N, and 6) P-to-N, respectively, and classified into two groups, i.e., the rising transients and the falling transients. Within the transients, the load current i_L is neglected because it crosses zero when the load is tuned at resonance, and i_{ZVS} is treated as constant because the dead-time period T_{dead} is much shorter than the pulse width of u_{AB}. The values of i_{ZVS} in the three types of rising transients are assumed to be identical and equal the minimum value $i_{\mathrm{ZVS\_min}}$. Similarly, the values of i_{ZVS} in the falling transients are assumed to equal the maximum value $i_{\mathrm{ZVS\_max}}$. Depending on $i_{\mathrm{ZVS\_min}}$ and $i_{\mathrm{ZVS\_max}}$, the six types of transients vary between four switching modes [10]: 1) post ZVS, 2) ideal ZVS, 3) partial ZVS, and 4) hard switching. The boundary current values are i_{optimal}, $-i_{\mathrm{optimal}}$, and 0, where i_{optimal} is the optimal current for ideal ZVS, i.e., the minimum current that can fully charge/discharge the switch output capacitances in a dead-time period

$$i_{\mathrm{optimal}} = \frac{2C_{\mathrm{OSSQ}}V_{\mathrm{dc}}}{T_{\mathrm{dead}}} \tag{1}$$

where C_{OSSQ} is the charge equivalent switch output capacitance, which is a function of the converter dc side voltage V_{dc} [19].

B. Dead-Time Voltage

As per Fig. 5(a)–(f), the integrals of u_{AB} during dead-time transients are functions of $i_{\mathrm{ZVS\_min}}$ and $i_{\mathrm{ZVS\_max}}$, and can be

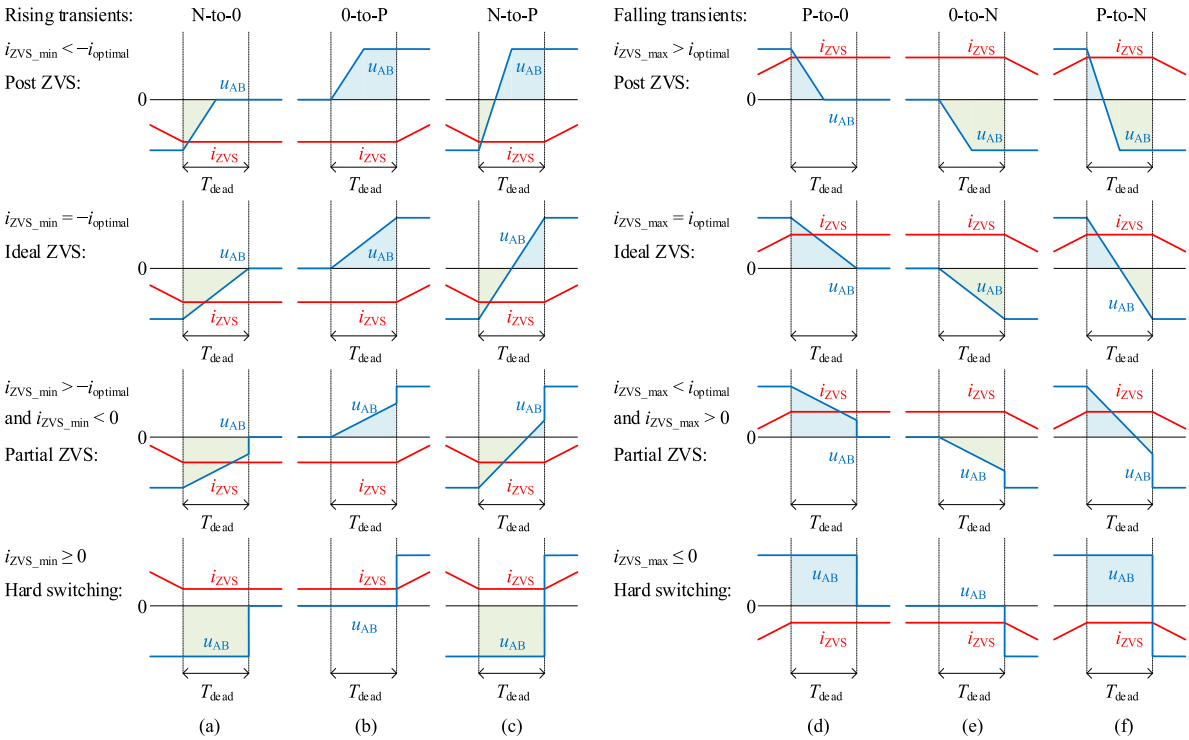

Fig. 5. Six types of dead-time transients and four switching modes.

expressed as

$$\int_{\mathrm{N-to-0}} u_{\mathrm{AB}}\,dt = \begin{cases} V_{\mathrm{dc}} T_{\mathrm{dead}} \dfrac{i_{\mathrm{optimal}}}{2i_{\mathrm{ZVS\_min}}} & \text{if } i_{\mathrm{ZVS\_min}} \leq -i_{\mathrm{optimal}} \\ -V_{\mathrm{dc}} T_{\mathrm{dead}} \left(\dfrac{i_{\mathrm{ZVS\_min}}}{2i_{\mathrm{optimal}}} + 1 \right) & \text{if } -i_{\mathrm{optimal}} < i_{\mathrm{ZVS\_min}} < 0 \\ -V_{\mathrm{dc}} T_{\mathrm{dead}} & \text{if } 0 \leq i_{\mathrm{ZVS\_min}} \end{cases} \tag{2}$$

$$\int_{\mathrm{0-to-P}} u_{\mathrm{AB}}\,dt = \begin{cases} V_{\mathrm{dc}} T_{\mathrm{dead}} \left(\dfrac{i_{\mathrm{optimal}}}{2i_{\mathrm{ZVS\_min}}} + 1 \right) & \text{if } i_{\mathrm{ZVS\_min}} \leq -i_{\mathrm{optimal}} \\ -V_{\mathrm{dc}} T_{\mathrm{dead}} \dfrac{i_{\mathrm{ZVS\_min}}}{2i_{\mathrm{optimal}}} & \text{if } -i_{\mathrm{optimal}} < i_{\mathrm{ZVS\_min}} < 0 \\ 0 & \text{if } 0 \leq i_{\mathrm{ZVS\_min}} \end{cases} \tag{3}$$

$$\int_{\mathrm{N-to-P}} u_{\mathrm{AB}}\,dt = \begin{cases} V_{\mathrm{dc}} T_{\mathrm{dead}} \left(\dfrac{i_{\mathrm{optimal}}}{i_{\mathrm{ZVS\_min}}} + 1 \right) & \text{if } i_{\mathrm{ZVS\_min}} \leq -i_{\mathrm{optimal}} \\ -V_{\mathrm{dc}} T_{\mathrm{dead}} \left(\dfrac{i_{\mathrm{ZVS\_min}}}{i_{\mathrm{optimal}}} + 1 \right) & \text{if } -i_{\mathrm{optimal}} < i_{\mathrm{ZVS\_min}} < 0 \\ -V_{\mathrm{dc}} T_{\mathrm{dead}} & \text{if } 0 \leq i_{\mathrm{ZVS\_min}} \end{cases} \tag{4}$$

$$\int_{\mathrm{P-to-0}} u_{\mathrm{AB}}\,dt = \begin{cases} V_{\mathrm{dc}} T_{\mathrm{dead}} \dfrac{i_{\mathrm{optimal}}}{2i_{\mathrm{ZVS\_max}}} & \text{if } i_{\mathrm{optimal}} \leq i_{\mathrm{ZVS\_max}} \\ -V_{\mathrm{dc}} T_{\mathrm{dead}} \left(\dfrac{i_{\mathrm{ZVS\_max}}}{2i_{\mathrm{optimal}}} - 1 \right) & \text{if } 0 < i_{\mathrm{ZVS\_max}} < i_{\mathrm{optimal}} \\ V_{\mathrm{dc}} T_{\mathrm{dead}} & \text{if } i_{\mathrm{ZVS\_max}} \leq 0 \end{cases} \tag{5}$$

$$\int_{\mathrm{0-to-N}} u_{\mathrm{AB}}\,dt = \begin{cases} V_{\mathrm{dc}} T_{\mathrm{dead}} \left(\dfrac{i_{\mathrm{optimal}}}{2i_{\mathrm{ZVS\_max}}} - 1 \right) & \text{if } i_{\mathrm{optimal}} \leq i_{\mathrm{ZVS\_max}} \\ -V_{\mathrm{dc}} T_{\mathrm{dead}} \dfrac{i_{\mathrm{ZVS\_max}}}{2i_{\mathrm{optimal}}} & \text{if } 0 < i_{\mathrm{ZVS\_max}} < i_{\mathrm{optimal}} \\ 0 & \text{if } i_{\mathrm{ZVS\_max}} \leq 0 \end{cases} \tag{6}$$

and

$$\int_{\mathrm{P-to-N}} u_{\mathrm{AB}}\,dt = \begin{cases} V_{\mathrm{dc}} T_{\mathrm{dead}} \left(\dfrac{i_{\mathrm{optimal}}}{i_{\mathrm{ZVS\_max}}} - 1 \right) & \text{if } i_{\mathrm{optimal}} \leq i_{\mathrm{ZVS\_max}} \\ -V_{\mathrm{dc}} T_{\mathrm{dead}} \left(\dfrac{i_{\mathrm{ZVS\_max}}}{i_{\mathrm{optimal}}} - 1 \right) & \text{if } 0 < i_{\mathrm{ZVS\_max}} < i_{\mathrm{optimal}} \\ V_{\mathrm{dc}} T_{\mathrm{dead}} & \text{if } i_{\mathrm{ZVS\_max}} \leq 0 \end{cases} \tag{7}$$

respectively. The average dead-time switch-node voltage $u_{\mathrm{AB\_Tdead\_avg}}$ is the sum of (2)–(7) weighed by their densities $d_{\mathrm{N-to-0}}$, $d_{\mathrm{0-to-P}}$, $d_{\mathrm{N-to-P}}$, $d_{\mathrm{P-to-0}}$, $d_{\mathrm{0-to-N}}$, and $d_{\mathrm{P-to-N}}$ over T_{dead}, i.e.,

$$\begin{aligned} u_{\mathrm{AB\_Tdead\_avg}} &= \frac{d_{\mathrm{N-to-0}}}{T_{\mathrm{dead}}}\int_{\mathrm{N-to-0}} u_{\mathrm{AB}}dt + \frac{d_{\mathrm{0-to-P}}}{T_{\mathrm{dead}}}\int_{\mathrm{0-to-P}} u_{\mathrm{AB}}dt \\ &+ \frac{d_{\mathrm{N-to-P}}}{T_{\mathrm{dead}}}\int_{\mathrm{N-to-P}} u_{\mathrm{AB}}dt + \frac{d_{\mathrm{P-to-0}}}{T_{\mathrm{dead}}}\int_{\mathrm{P-to-0}} u_{\mathrm{AB}}dt \\ &+ \frac{d_{\mathrm{0-to-N}}}{T_{\mathrm{dead}}}\int_{\mathrm{0-to-N}} u_{\mathrm{AB}}dt + \frac{d_{\mathrm{0-to-N}}}{T_{\mathrm{dead}}}\int_{\mathrm{0-to-N}} u_{\mathrm{AB}}dt. \end{aligned} \tag{8}$$

Equation (8) can be simplified as

$$u_{\mathrm{AB\_Tdead\_avg}} = \frac{d}{2T_{\mathrm{dead}}}\left(\int_{\mathrm{N-to-P}} u_{\mathrm{AB}}\mathrm{d}t + \int_{\mathrm{P-to-N}} u_{\mathrm{AB}}\mathrm{d}t\right) \tag{9}$$

by using the relationships of

$$\begin{cases} \int_{\mathrm{N-to-P}} u_{\mathrm{AB}}dt = \int_{\mathrm{N-to-0}} u_{\mathrm{AB}}dt + \int_{\mathrm{0-to-P}} u_{\mathrm{AB}}dt \\ \int_{\mathrm{P-to-N}} u_{\mathrm{AB}}dt = \int_{\mathrm{P-to-0}} u_{\mathrm{AB}}dt + \int_{\mathrm{0-to-N}} u_{\mathrm{AB}}dt \end{cases} \tag{10}$$

and

$$\begin{cases} d_{\mathrm{0-to-P}} + d_{\mathrm{N-to-P}} = d_{\mathrm{0-to-N}} + d_{\mathrm{P-to-N}} = \dfrac{d}{2} \\ d_{\mathrm{P-to-0}} + d_{\mathrm{P-to-N}} = d_{\mathrm{N-to-0}} + d_{\mathrm{N-to-P}} = \dfrac{d}{2} \end{cases} \tag{11}$$

where (10) are directly derived from (2)–(7), (11) are derived from the PDM rules that the positive and negative pulses in u_{AB} occur alternately and the total pulse density equals the specified d [18].

In (4) and (7), $i_{\mathrm{ZVS\_min}}$ and $i_{\mathrm{ZVS\_max}}$ can be expressed by the midrange ZVS current $i_{\mathrm{ZVS\_mid}}$ and the peak-to-peak ZVS current Δi_{ZVS} as

$$\begin{cases} i_{\mathrm{ZVS\_min}} = i_{\mathrm{ZVS\_mid}} - \dfrac{\Delta i_{\mathrm{ZVS}}}{2} \\ i_{\mathrm{ZVS\_max}} = i_{\mathrm{ZVS\_mid}} + \dfrac{\Delta i_{\mathrm{ZVS}}}{2}. \end{cases} \tag{12}$$

Δi_{ZVS} is determined by the relationship of

$$L_{\mathrm{ZVS}}\Delta i_{\mathrm{ZVS}} = \frac{V_{\mathrm{dc}}T_s}{2} \tag{13}$$

where T_s is the fundamental switching period, i.e., the switching period when $d = 1$. When the ZVS inductance is optimized as [19]

$$L_{\mathrm{ZVS}} = \frac{T_s T_{\mathrm{dead}}}{8C_{\mathrm{OSSQ}}} \tag{14}$$

Δi_{ZVS} is twice of i_{optimal}, i.e.,

$$\Delta i_{\mathrm{ZVS}} = 2i_{\mathrm{optimal}} \tag{15}$$

and (12) becomes

$$\begin{cases} i_{\mathrm{ZVS\_min}} = i_{\mathrm{ZVS\_mid}} - i_{\mathrm{optimal}} \\ i_{\mathrm{ZVS\_max}} = i_{\mathrm{ZVS\_mid}} + i_{\mathrm{optimal}}. \end{cases} \tag{16}$$

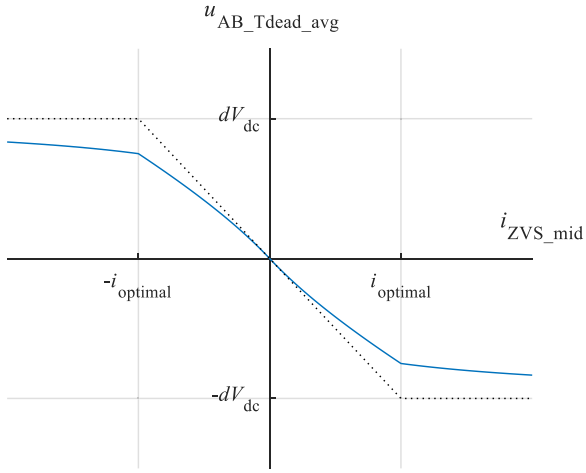

Fig. 6. $u_{\mathrm{AB\_Tdead\_avg}}$ as a function of $i_{\mathrm{ZVS\_mid}}$.

Using the expressions of (16) and substituting (4) and (7) into (9), $u_{\mathrm{AB\_Tdead\_avg}}$ is written as a function of $i_{\mathrm{ZVS\_mid}}$, namely

$$u_{\mathrm{AB\_Tdead\_avg}} = -\frac{dV_{\mathrm{dc}}}{2} \times \left[\frac{i_{\mathrm{ZVS\_mid}}}{|i_{\mathrm{ZVS\_mid}}| + i_{\mathrm{optimal}}} + \frac{i_{\mathrm{ZVS\_mid}}}{\max\left(i_{\mathrm{optimal}}, |i_{\mathrm{ZVS\_mid}}|\right)}\right]. \tag{17}$$

Fig. 6 shows the relationship between $u_{\mathrm{AB\_Tdead\_avg}}$ and $i_{\mathrm{ZVS\_mid}}$ described by (17). The slope at origin is derived from (17) as

$$\left.\frac{du_{\mathrm{AB\_Tdead\_avg}}}{di_{\mathrm{ZVS\_mid}}}\right|_{(0,0)} = -\frac{dV_{\mathrm{dc}}}{i_{\mathrm{optimal}}}. \tag{18}$$

C. Negative Feedback Effect

Since the densities of the positive and negative pulses in u_{AB} are equal, the average of u_{AB} depends only on $u_{\mathrm{AB\_Tdead\_avg}}$

$$u_{\mathrm{AB\_avg}} = \frac{2T_{\mathrm{dead}}}{T_s}u_{\mathrm{AB\_Tdead\_avg}}. \tag{19}$$

The average ZVS current $i_{\mathrm{ZVS\_avg}}$ may differ from $i_{\mathrm{ZVS\_mid}}$, depending on the shape of i_{ZVS}

$$i_{\mathrm{ZVS\_avg}} = i_{\mathrm{ZVS\_mid}} + C_{\mathrm{shape}}\Delta i_{\mathrm{ZVS}} \tag{20}$$

where C_{shape} is a shape coefficient. For example, the current waveform shown in Fig. 4 has a $C_{\mathrm{shape}} = -0.25$.

In a ZVS full-bridge converter without C_b, the dynamical relationship between $u_{\mathrm{AB\_avg}}$ and $i_{\mathrm{ZVS\_avg}}$ can be described by the averaged differential equation

$$L_{\mathrm{ZVS}}\frac{\mathrm{d}i_{\mathrm{ZVS\_avg}}}{\mathrm{d}t} + R_{\mathrm{ZVS}}i_{\mathrm{ZVS\_avg}} = u_{\mathrm{AB\_avg}}. \tag{21}$$

With (18)–(20), (21) can approximately be transformed as

$$\begin{aligned} &L_{\mathrm{ZVS}}\frac{\mathrm{d}i_{\mathrm{ZVS\_mid}}}{\mathrm{d}t} + \left(R_{\mathrm{ZVS}} + \frac{2dV_{\mathrm{dc}}T_{\mathrm{dead}}}{i_{\mathrm{optimal}}T_s}\right) \\ &i_{\mathrm{ZVS\_mid}} \approx -R_{\mathrm{ZVS}}C_{\mathrm{shape}}\Delta i_{\mathrm{ZVS}} \end{aligned} \tag{22}$$

TABLE I
CONVERTER PARAMETERS

Symbol	Quantity	Value
V_{dc}	Converter dc side voltage	40 V
T_{dead}	Dead time period	50 ns
C_{OSSQ}	Charge equivalent switch output capacitance	600 pF
$i_{optimal}$	Optimal current for ideal ZVS	1 A
T_s	Fundamental switching period	1 μs
f_s	Fundamental switching frequency	1 MHz
L_{ZVS}	ZVS inductance	10 μH
Δi_{ZVS}	Peak-to-peak ZVS current	2 A
R_{ZVS}	ZVS branch resistance	< 0.2 Ω
τ_{ZVS}	ZVS time constant	< 0.12 ns

Switching device model: EPC2010C.

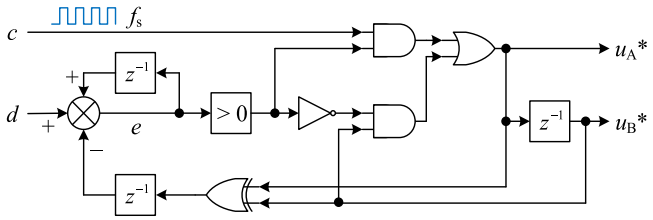

Fig. 7. Block diagram of the proposed PDM strategy.

where Δi_{ZVS} is treated as constant. In (22), the dead-time voltage provides an additional negative feedback term that pushes i_{ZVS_mid} toward the steady-state value

$$i_{ZVS\_mid} \approx \frac{-C_{shape}}{1+\frac{2dV_{dc}T_{dead}}{R_{ZVS}i_{optimal}T_s}}\Delta i_{ZVS}. \tag{23}$$

By using (1), (23) can be simplified as

$$i_{ZVS\_mid} \approx \frac{-C_{shape}}{1+\frac{dT_{dead}{}^2}{\tau_{ZVS}T_s}}\Delta i_{ZVS} \tag{24}$$

where τ_{ZVS} is the ZVS time constant

$$\tau_{ZVS} = R_{ZVS}C_{OSSQ}. \tag{25}$$

The right-hand side of (24) can be very close to zero, and it explains the waveforms shown in Fig. 4. The waveforms were obtained with $d = 0.5$, $C_{shape} = -0.25$, and the other parameters listed in Table I. As per the parameters and (24), the absolute i_{ZVS_mid} is smaller than 45 mA, which is negligible as compared with Δi_{ZVS}. Therefore, $i_{ZVS\_min} \approx -\Delta i_{ZVS}/2 = -1$ A $= -i_{optimal}$ and $i_{ZVS\_max} \approx \Delta i_{ZVS}/2 = 1$ A $= i_{optimal}$, meeting the conditions for the ideal ZVS. Meanwhile, $i_{ZVS\_avg} \approx C_{shape}\Delta i_{ZVS} = -0.5$ A, as shown in Fig. 4.

III. PROPOSED PDM STRATEGY

A. Operating Principle

Utilizing the negative feedback effect of the dead-time voltage, a simplified PDM strategy that allows asymmetric ZVS currents is proposed for the ZVS full-bridge converters without dc blocking capacitors. The block diagram of the strategy is shown in Fig. 7. The input signals include a continuous pulse c and a specified pulse density d. The frequency of c equals the fundamental switching frequency $f_s = 1/T_s$. The range of d is [0, 1]. The output signals are u_A^* and u_B^*, which are the references for the switch nodes A and B, respectively. The strategy uses an adder, a comparator, five logic gates, and three delay units. The delay units are triggered by the rising and falling edges of c. Therefore, the iteration frequency of the strategy is $2f_s$. In each iteration, the difference between d and u_A^* XOR u_B^* is accumulated and the result is denoted by e. If $e > 0$, u_A^* equals c, otherwise equals the previous u_A^*. u_B^* always equals the previous u_A^*. The overall operation of the strategy can be described by a set of difference equations

$$\begin{cases} e[n] = e[n-1] + d[n] - u_A^*[n-1] \oplus u_B^*[n-1] \\ u_A^*[n] = e[n] > 0 \wedge c[n] \vee \neg e[n] > 0 \wedge u_A^*[n-1] \\ u_B^*[n] = u_A^*[n-1] \end{cases} \tag{26}$$

where n is the index of the iterations, "∧," "∨," "¬,"and "⊕" are the logic symbols of AND, OR, NOT, and XOR, respectively. Fig. 8 shows the ideal waveforms when $d = 0.5$ as an example.

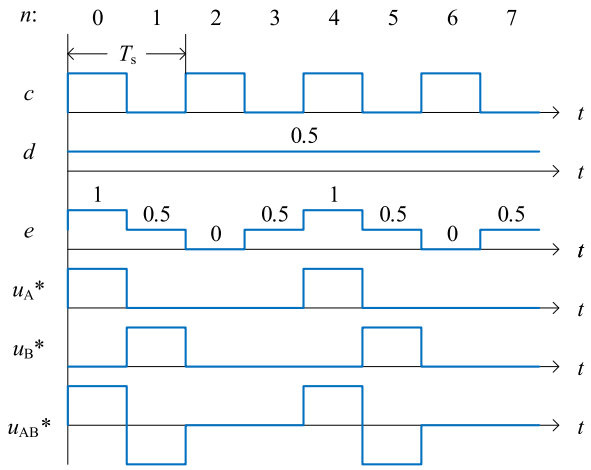

Fig. 8. Ideal waveforms of the proposed PDM strategy when $d = 0.5$.

B. ZVS Current Analysis

When using the proposed PDM strategy, i_{ZVS} and C_{shape} vary with d, as the examples shown in Table II. More generally, when d is a rational number that can be expressed as the quotient of two coprime integers p and q, i.e.,

$$d = \frac{p}{q} \tag{27}$$

there exists a minimum modulation period qT_s, and C_{shape} can be calculated in qT_s and expressed as

$$C_{shape} = \pm\frac{\mathrm{mod}\,(q-p,2)}{2q} \tag{28}$$

where the sign of C_{shape} depends on the initial value of e. When d is an irrational number, there is no modulation period, and C_{shape} approaches to 0 when the period for calculation extends to infinity. The relationship between C_{shape} and d is shown in Fig. 9.

TABLE II
MODULATION EXAMPLES

d	Modulation period	Waveforms of u_{AB} and i_{ZVS}	C_{shape}
1	T_s		0
1/2	$2T_s$	or	±1/4
1/3	$3T_s$		0
2/3	$3T_s$	or	±1/6

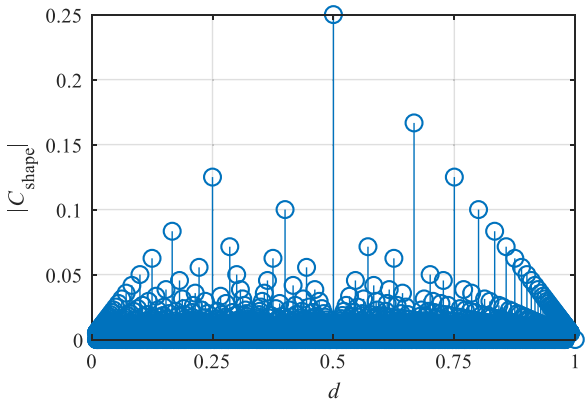

Fig. 9. C_{shape} versus d when using the proposed PDM strategy.

As per (28) and Fig. 9, for any d within (0, 1], the absolute C_{shape} is limited by

$$|C_{shape}| \le \begin{cases} \dfrac{d}{2} & \text{if} \quad 0 < d \le 0.5 \\ \dfrac{1-d}{2} & \text{if} \quad 0.5 < d \le 1. \end{cases} \tag{29}$$

By substituting (29) into (24), the range of $|i_{ZVS\_mid}|$ for any d within (0, 1] is obtained

$$|i_{ZVS\_mid}| \le \frac{0.25}{1 + \frac{0.5T_{dead}{}^2}{\tau_{ZVS} T_s}} \Delta i_{ZVS} \tag{30}$$

where the equality holds when $d = 0.5$. Therefore, with a suitable relationship between τ_{ZVS}, T_{dead}, and T_s, the proposed PDM strategy can ensure that $i_{ZVS\_mid} \approx 0$ as compared with Δi_{ZVS}, and achieve the ideal ZVS for any d.

IV. EXPERIMENTS OF A STANDALONE CONVERTER

To verify the advantages of the proposed PDM strategy over the existing one, the two strategies were adopted in the same gallium-nitride (GaN) device-based ZVS full-bridge converter for comparison. The converter was described in [18] and shown in Fig. 10. The parameters are listed in Table I. The dc blocking capacitor on the ZVS branch was removed for both strategies.

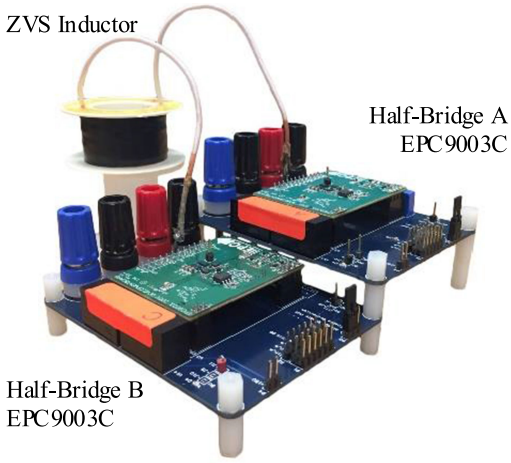

Fig. 10. Experimental ZVS full-bridge converter [18].

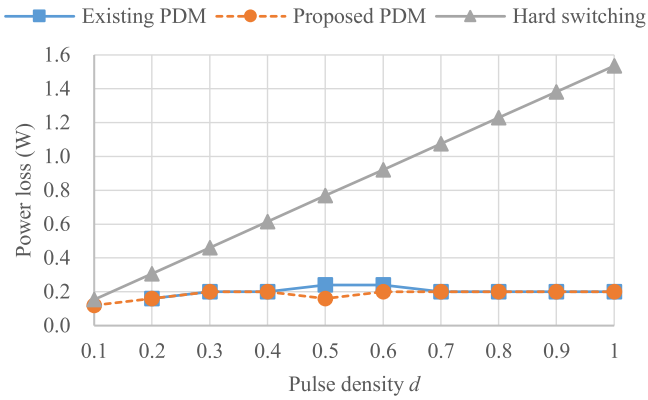

Fig. 11. Measured converter power losses versus calculated hard switching losses.

A. Steady-State Performances

The steady-state performances of the converter were tested to confirm the ZVS operation and investigate the subharmonics of u_{AB}. As shown in Fig. 11, the measured power losses of the converter with different d were about 0.2 W, which were much lower than the calculated hard switching power losses, indicating that the ZVS was achieved by both the PDM strategies. Fig. 12 shows the measured waveforms when $d = 0.5$ as an example. Fig. 13 compares the subharmonics of $|u_{AB}|$ with normalized units. $|u_{AB}|$ is of interest because the positive and negative pulses of u_{AB} are equally effective when driving a resonant load. The dc component of $|u_{AB}|$ equaled the specified d for both the PDM strategies, while the low-frequency subharmonic at $0.25 f_s$ was eliminated by the proposed one. As the remaining subharmonics were concentrated closer to f_s, the power flow can be controlled more smoothly and the electromagnetic interferences can be suppressed more easily. Similar results were also obtained with different d.

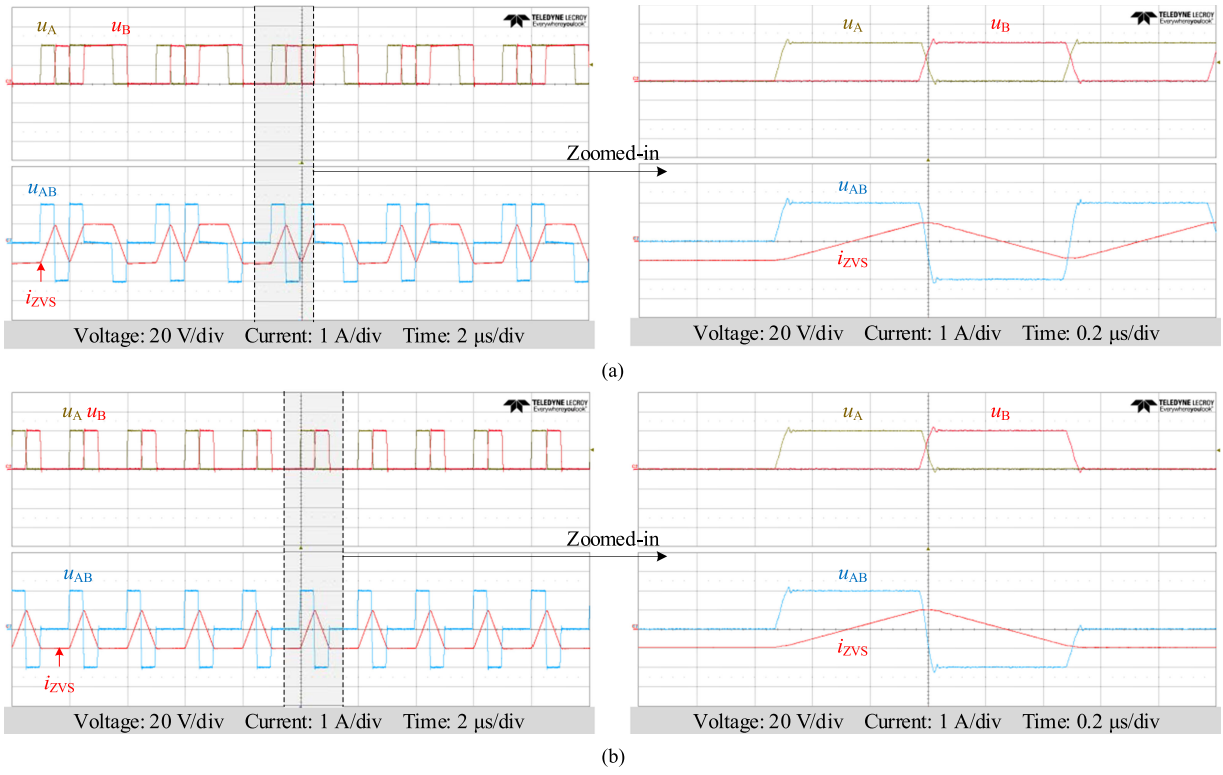

Fig. 12. Steady-State waveforms when $d = 0.5$, using (a) the existing and (b) the proposed PDM strategies.

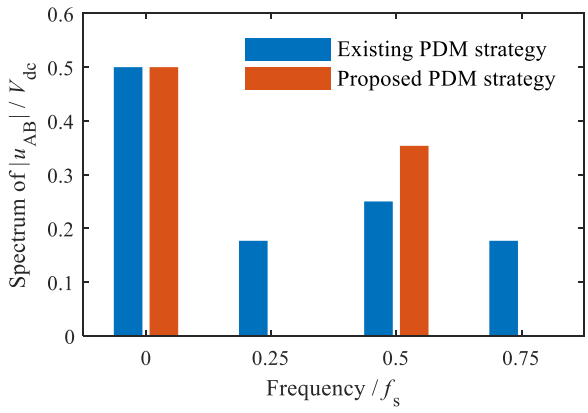

Fig. 13. Subharmonic spectrum of $|u_{AB}|$ when $d = 0.5$.

B. Sinusoidal Responses

The sinusoidal responses of the converter were tested to investigate the range of the achievable d. Fig. 14 shows the measured responses when the specified $d = 0.5 + 0.5 \sin(4000\pi t)$, i.e., a biased 2 kHz sine wave with a maximum of 1 and a minimum of 0. The existing PDM strategy needed an appropriate lower limit on d to ensure the stability and continuous operation, while the proposed one could accurately follow the specified d, covering the full range of [0, 1].

C. Step Responses

The step responses of the converter were tested to investigate the modulation delay. Fig. 15 shows the measured responses when the specified d steps between 0.2 (the lower limit of the existing PDM strategy) and 1. With the existing PDM strategy, the modulation delays were about 4 μs ($4T_s$) and 10 μs ($10T_s$) for the step up and down, respectively, depending on the accumulation coefficient k_e. In contrast, u_{AB} responded to the changes of d immediately when using the proposed PDM strategy. The fast response can simplify the system level dynamical analysis and control [20]–[22] as the modulation can be treated as ideal.

V. Experiments of a WPT System

The proposed PDM strategy was further tested in a WPT system with dual-side PDM ZVS full-bridge converters, as shown in Fig. 16. The circuit diagram of the system is shown in Fig. 17. The parameters are listed in Table III. The transmitting side converter operates as an inverter that injects energy to the transmitter resonator, whose inductance, capacitance, and ESR are denoted by L_1, C_1, and R_1, respectively. The receiving side converter operates as a synchronous rectifier that absorbs energy from the receiver resonator, whose inductance, capacitance, and ESR are denoted by L_2, C_2, and R_2, respectively. The pulse densities of the two converters are denoted by d_1 and d_2, respectively. The fundamental switching frequency was slightly adjusted to match with the resonant frequency.

A. Steady-State Performances

The steady-state performances of the system were tested at three operating points as listed in Table IV. The corresponding waveforms are shown in Fig. 18. For all the three operating

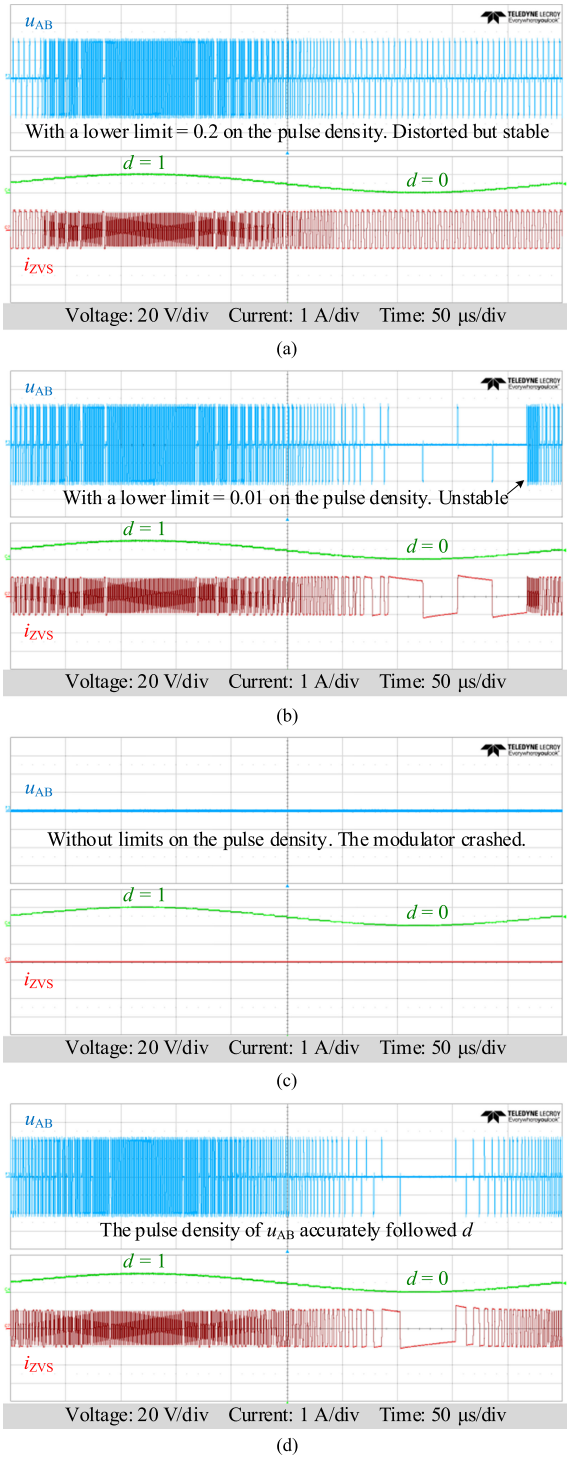

Fig. 14. Sinusoidal responses when $d = 0.5 + 0.5 \sin(4000\pi t)$, using (a) the exiting PDM strategy with a lower limit = 0.2 on d, (b) the exiting PDM strategy with a lower limit = 0.01 on d, (c) the exiting PDM strategy without limits on d, and (d) the proposed PDM strategy.

points, the input dc voltage of the system was fixed at 40 V, and the pulse densities d_1 and d_2 were adjusted to achieve a unity dc voltage gain with the highest system efficiency from dc input to dc output. The efficiency was higher than 90% when the power transfer distance was 15 cm, i.e., half of the coil diameter, and was higher than 80% when the distance was doubled.

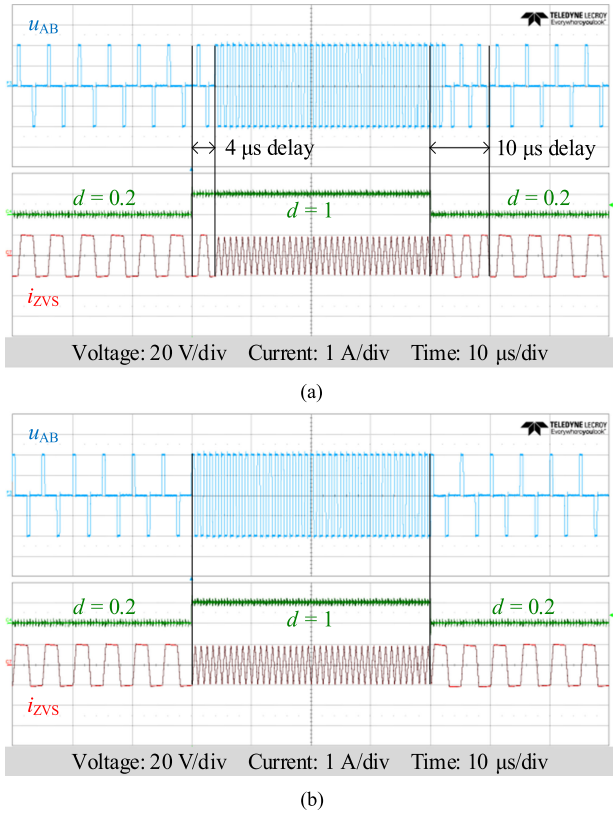

Fig. 15. Step responses when d steps between 0.2 and 1, using (a) the existing and (b) the proposed PDM strategies.

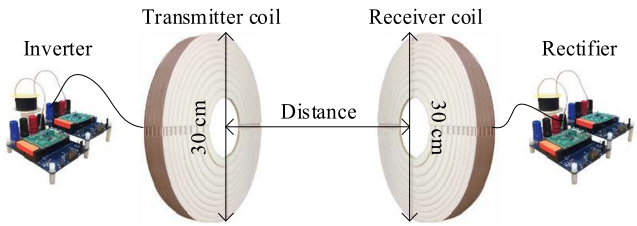

Fig. 16. Experimental WPT system [18].

TABLE III
WPT SYSTEM PARAMETERS

Symbol	Quantity	Value
$L_{1,2}$	Resonant inductances	75.3 µH
$C_{1,2}$	Resonant capacitances	400 pF
$f_{r1,2}$	Resonant frequencies	0.917 MHz
f_s	Fundamental switching frequency	0.917 MHz

B. Sinusoidal Responses

Under the conditions of 40 V input dc voltage, 30 cm power transfer distance, and 100 Ω load resistance, Fig. 19(a) and (b) shows the system sinusoidal responses when $d_1 = 0.5 + 0.5 \sin(4000\pi t)$, $d_2 = 0.5$ and $d_1 = 0.5$, $d_2 = 0.5 + 0.5 \sin(4000\pi t)$, respectively. For both the cases, the pulse densities of the switch-node voltages u_{AB1} and u_{AB2} accurately followed the specified d_1 and d_2, respectively. The midrange ZVS currents were always maintained near zero so that the ZVS operation of

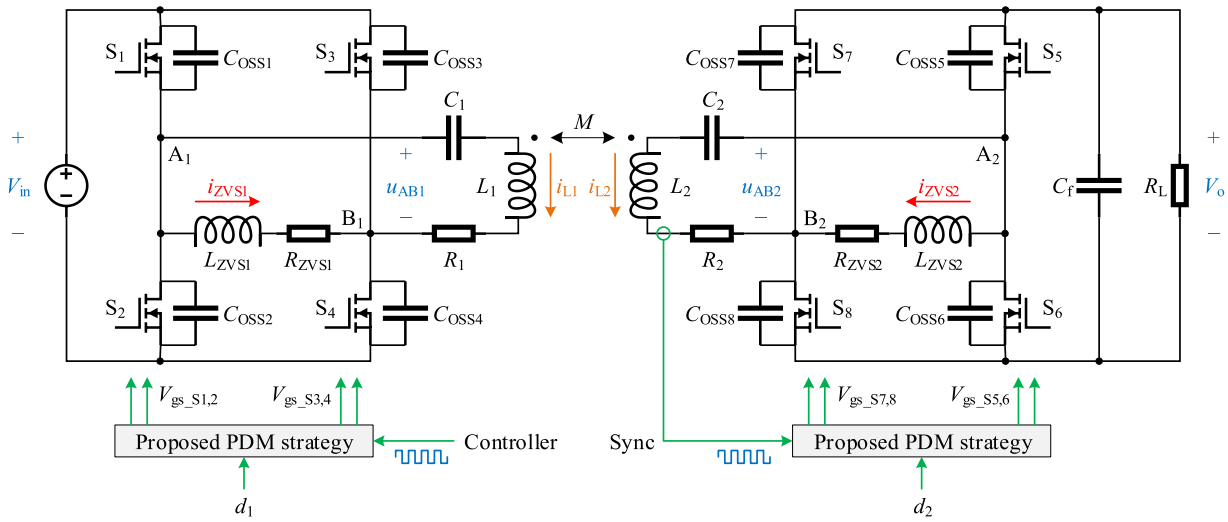

Fig. 17. Circuit diagram of the experimental WPT system.

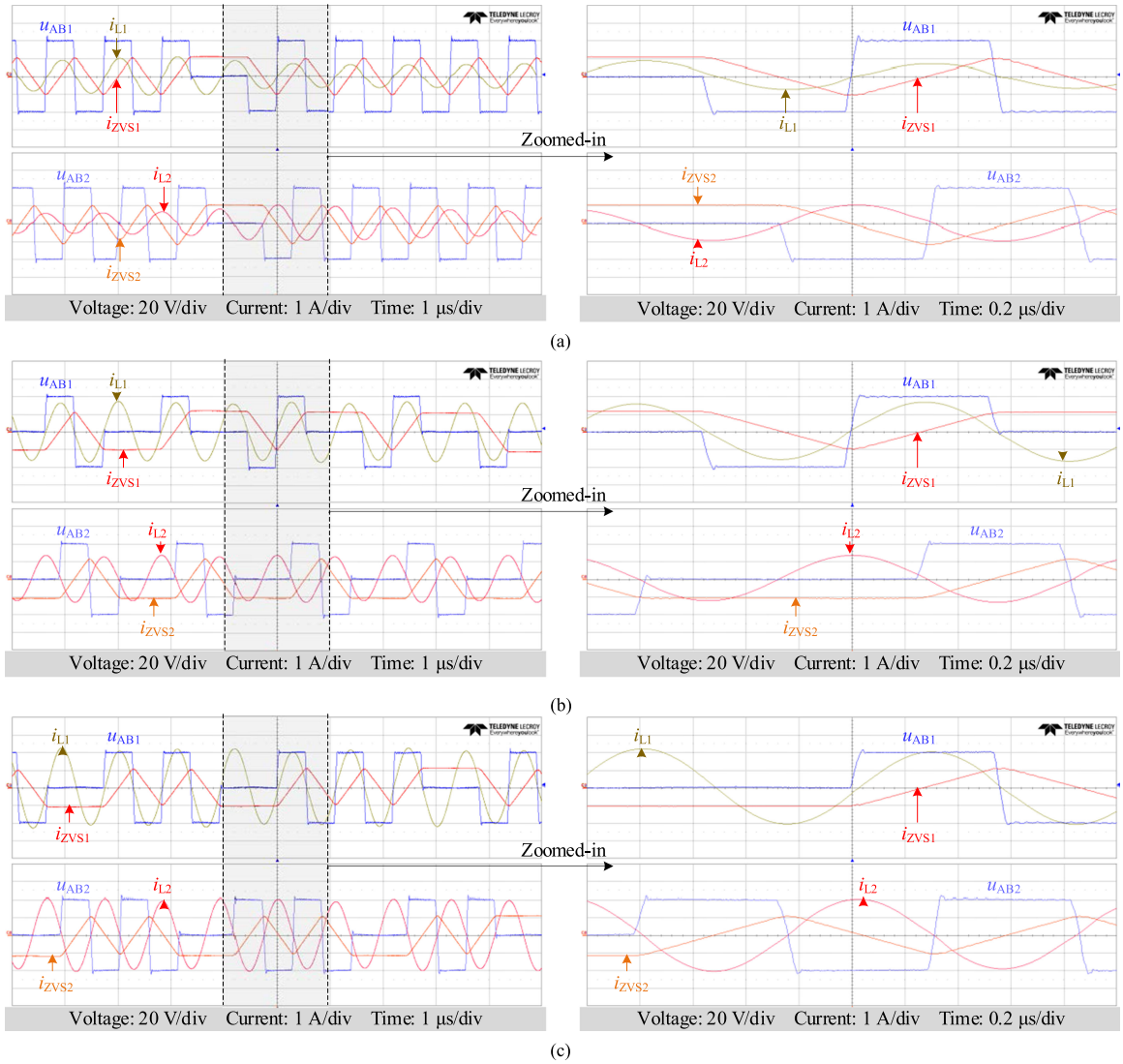

Fig. 18. Waveforms at three steady-state operating points. (a) Distance = 15 cm, load resistance = 100 Ω. (b) Distance = 30 cm, load resistance = 100 Ω. (c) Distance = 30 cm, load resistance = 50 Ω.

TABLE IV
OPERATING POINTS

Distance	Load resistance	Input dc voltage	d_1	d_2	Output dc voltage	Input dc power	Output dc power	System efficiency
15 cm	100 Ω	40 V	0.890	0.90	40 V	17.5 W	16.0 W	91 %
30 cm	100 Ω	40 V	0.465	0.50	40 V	19.6 W	16.0 W	82 %
30 cm	50 Ω	40 V	0.708	0.65	40 V	39.1 W	32.1 W	82 %

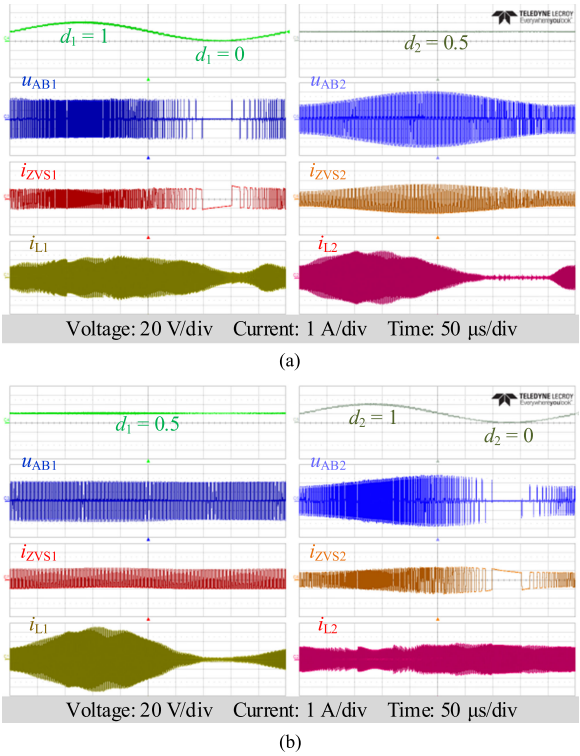

Fig. 19. Sinusoidal responses under the conditions of 40 V input dc voltage, 30 cm power transfer distance, and 100 Ω load resistance when (a) $d_1 = 0.5 + 0.5 \sin(4000\pi t)$, $d_2 = 0.5$, and (b) $d_1 = 0.5$, $d_2 = 0.5 + 0.5 \sin(4000\pi t)$.

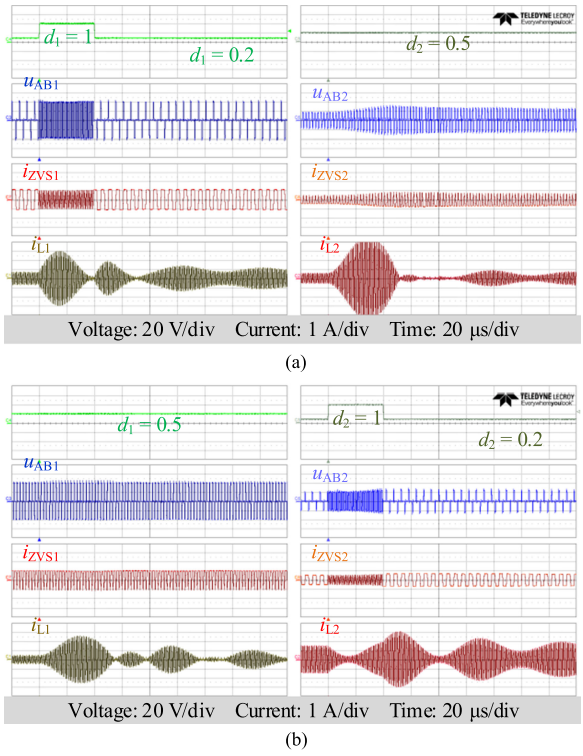

Fig. 20. Step responses under the conditions of 40 V input dc voltage, 30 cm power transfer distance, and 100 Ω load resistance when (a) d_1 steps between 0.2 and 1, $d_2 = 0.5$, and (b) $d_1 = 0.5$, d_2 steps between 0.2 and 1.

the converters was ensured. The sinusoidal d_1 and d_2 leaded to the changes of resonant current envelopes, as well as the changes of the envelope of u_{AB2}.

C. Step Responses

Under the same conditions as the sinusoidal test, Fig. 20(a) and (b) shows the system step responses when d_1 steps between 0.2 and 1, $d_2 = 0.5$, and $d_1 = 0.5$, d_2 steps between 0.2 and 1, respectively. For both the cases, the switch-node voltages u_{AB1} and u_{AB2} responded to the changes of d_1 and d_2 immediately, and triggered complex dynamic processes. Consequently, the system dynamical behaviors can be well studied on this experimental platform.

VI. Conclusion

In a ZVS full-bridge converter, the switch-node voltage in dead-time transients depends on the ZVS current. The average switch-node voltage in multiple dead-time transients can provide a strong negative feedback effect that pushes the midrange ZVS current toward zero regardless of its average value so that the ideal ZVS can be ensured even with an asymmetric ZVS current. This effect is utilized by the proposed PDM strategy to overcome the limitations of the existing PDM strategy for ZVS full-bridge converters. As compared with the existing one, the proposed PDM strategy exhibits lower low-frequency subharmonics, wider modulation range, and faster response. With these advantages, PDM ZVS full-bridge converters can be one of the ideal choices for WPT systems.

References

[1] C. T. Rim and C. Mi, *Wireless Power Transfer for Electric Vehicles and Mobile Devices*. Hoboken, NJ, USA: Wiley, 2017.
[2] A. Daga, J. M. Miller, B. R. Long, R. Kacergis, P. Schrafel, and J. Wolgemuth, "Electric fuel pumps for wireless power transfer: Enabling rapid growth in the electric vehicle market," *IEEE Power Electron. Mag.*, vol. 4, no. 2, pp. 24–35, Jun. 2017.
[3] C. C. Mi, G. Buja, S. Y. Choi, and C. T. Rim, "Modern advances in wireless power transfer systems for roadway powered electric vehicles," *IEEE Trans. Ind. Electron.*, vol. 63, no. 10, pp. 6533–6545, Oct. 2016.
[4] S. Y. Choi, B. W. Gu, S. Y. Jeong, and C. T. Rim, "Advances in wireless power transfer systems for roadway-powered electric vehicles," *IEEE J. Emerg. Sel. Topics Power Electron.*, vol. 3, no. 1, pp. 18–36, Mar. 2015.
[5] G. A. Covic and J. T. Boys, "Modern trends in inductive power transfer for transportation applications," *IEEE J. Emerg. Sel. Topics Power Electron.*, vol. 1, no. 1, pp. 28–41, Mar. 2013.

[6] S. Y. R. Hui, W. X. Zhong, and C. K. Lee, "A critical review of recent progress in mid-range wireless power transfer," *IEEE Trans. Power Electron.*, vol. 29, no. 9, pp. 4500–4511, Sep. 2014.
[7] G. A. Covic and J. T. Boys, "Inductive power transfer," *Proc. IEEE*, vol. 101, no. 6, pp. 1276–1289, Jun. 2013.
[8] J. T. Boys and G. A. Covic, "The inductive power transfer story at the University of Auckland," *IEEE Circuits Syst. Mag.*, vol. 15, no. 2, pp. 6–27, Apr.–Jun. 2015.
[9] J. M. Miller, P. T. Jones, J. M. Li, and O. C. Onar, "ORNL experience and challenges facing dynamic wireless power charging of EV's," *IEEE Circuits Syst. Mag.*, vol. 15, no. 2, pp. 40–53, Apr.–Jun. 2015.
[10] M. A. de Rooij and Y. Zhang, "eGaN FET based 6.78 MHz differential-mode ZVS class D AirFuel class 4 wireless power amplifier," in *Proc. Int. Exhib. Conf. Power Electron., Intell. Motion, Renewable Energy Energy Manage.*, 2016, pp. 1–8.
[11] H. Li, J. Li, K. Wang, W. Chen, and X. Yang, "A maximum efficiency point tracking control scheme for wireless power transfer systems using magnetic resonant coupling," *IEEE Trans. Power Electron.*, vol. 30, no. 7, pp. 3998–4008, Jul. 2015.
[12] H. Li, J. Fang, S. Chen, K. Wang, and Y. Tang, "Pulse density modulation for maximum efficiency point tracking of wireless power transfer systems," *IEEE Trans. Power Electron.*, vol. 33, no. 6, pp. 5492–5501, Jun. 2018.
[13] M. Fu, H. Yin, M. Liu, and C. Ma, "Loading and power control for a high-efficiency class E PA-driven megahertz WPT system," *IEEE Trans. Ind. Electron.*, vol. 63, no. 11, pp. 6867–6876, Nov. 2016.
[14] X. Dai, X. Li, Y. Li, and A. P. Hu, "Maximum efficiency tracking for wireless power transfer systems with dynamic coupling coefficient estimation," *IEEE Trans. Power Electron.*, vol. 33, no. 6, pp. 5005–5015, Jun. 2018.
[15] W. Zhong and S. Y. R. Hui, "Maximum energy efficiency operation of series-series resonant wireless power transfer systems using on-off keying modulation," *IEEE Trans. Power Electron.*, vol. 33, no. 4, pp. 3595–3603, Apr. 2018.
[16] Z. Huang, S.-C. Wong, and C. K. Tse, "Control design for optimizing efficiency in inductive power transfer systems," *IEEE Trans. Power Electron.*, vol. 33, no. 5, pp. 4523–4534, May 2018.
[17] M. F. Fu, H. Yin, X. E. Zhu, and C. B. Ma, "Analysis and tracking of optimal load in wireless power transfer systems," *IEEE Trans. Power Electron.*, vol. 30, no. 7, pp. 3952–3963, Jul. 2015.
[18] H. Li, K. Wang, J. Fang, and Y. Tang, "Pulse density modulated ZVS full-bridge converters for wireless power transfer systems," *IEEE Trans. Power Electron.*, vol. 34, no. 1, pp. 369–377, Jan. 2019.
[19] M. A. de Rooij, "The ZVS voltage-mode class-D amplifier, an eGaN FET-enabled topology for highly resonant wireless energy transfer," in *Proc. IEEE Appl. Power Electron. Conf. Expo.*, 2015, pp. 1608–1613.
[20] A. P. Hu, "Modeling a contactless power supply using GSSA method," in *Proc. IEEE Int. Conf. Ind. Technol.*, 2009, pp. 1–6.
[21] Z. U. Zahid, Z. Dalala, and J. S. J. Lai, "Small-Signal modeling of series-series compensated induction power transfer system," in *Proc. IEEE Appl. Power Electron. Conf. Expo.*, 2014, pp. 2847–2853.
[22] H. Li, K. Wang, L. Huang, W. Chen, and X. Yang, "Dynamic modeling based on coupled modes for wireless power transfer systems," *IEEE Trans. Power Electron.*, vol. 30, no. 11, pp. 6245–6253, Nov. 2015.

Hongchang Li (S'12–M'16) received the B.Eng. and D.Eng. degrees in electrical engineering from Xi'an Jiaotong University, Xi'an, China, in 2011 and 2016, respectively.

From August 2014 to August 2015, he was a Visiting Scholar with Lawrence Berkeley National Laboratory, Berkeley, CA, USA. He is currently a Research Fellow with the Energy Research Institute, Nanyang Technological University, Singapore. His research interests include wireless power transfer, electron tomography, and distributed energy storage systems.

Dr. Li was a recipient of the Best Paper Award of IEEE Southern Power Electronics Conference in 2018.

Shuxin Chen (S'17) received the B.Eng. degree in electronic engineering from the Hong Kong Polytechnic University, Hong Kong, in 2015, the bachelor's degree in microelectronic engineering from the Sun Yet-Sen University, Guangzhou, China, in 2015, and the M.Sc. degree in power engineering from Nanyang Technological University, Singapore, in 2016. He is currently working toward the Ph.D. degree in electrical and electronic engineering with Nanyang Technological University.

His current research interests include wireless power transfer and power converter control.

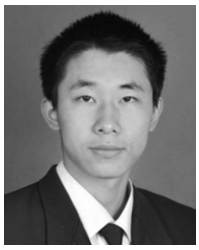

Jingyang Fang (S'15) received the B.Sc. and M.Sc. degrees in electrical engineering from Xi'an Jiaotong University, Xi'an, China, in 2013 and 2015, respectively, and the Ph.D. degree from the School of Electrical and Electronic Engineering, Nanyang Technological University, Singapore, in 2018.

From May 2018 to August 2018, he was a Visiting Scholar with the Institute of Energy Technology, Aalborg University, Aalborg, Denmark. He is currently a Research Fellow with the School of Electrical and Electronic Engineering, Nanyang Technological University, Singapore. He has authored or coauthored more than 40 papers in the fields of power electronics and its applications. His research interests include power quality control, stability analysis and improvement, renewable energy integration, and digital control in more-electronics power systems.

Dr. Fang was a recipient of the Best Paper Award of Asia Conference on Energy, Power, and Transportation Electrification in 2017 and a recipient of the Best Presenter of 2018 IEEE International Power Electronics and Application Conference and Exposition in 2018.

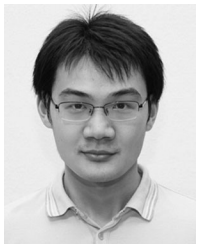

Yi Tang (S'10−M'14−SM'18) received the B.Eng. degree in electrical engineering from Wuhan University, Wuhan, China, in 2007, and the M.Sc. and Ph.D. degrees from the School of Electrical and Electronic Engineering, Nanyang Technological University, Singapore, in 2008 and 2011, respectively.

From 2011 to 2013, he was a Senior Application Engineer with Infineon Technologies Asia Pacific, Singapore. From 2013 to 2015, he was a Post-Doctoral Research Fellow with Aalborg University, Aalborg, Denmark. Since March 2015, he has been with Nanyang Technological University as an Assistant Professor. He is the Cluster Director of the Advanced Power Electronics Research Program, Energy Research Institute, Nanyang Technological University.

Dr. Tang was a recipient of the Infineon Top Inventor Award in 2012, the Early Career Teaching Excellence Award in 2017, and four IEEE Prize Paper Awards. He was an Associate Editor for the IEEE TRANSACTIONS ON POWER ELECTRONICS and the IEEE JOURNAL OF EMERGING AND SELECTED TOPICS IN POWER ELECTRONICS.

Michael A. de Rooij (SM'03) received the B.Eng., M.Eng., and D.Eng. degrees in electronics and electrical engineering with major in power electronics from the Rand Afrikaans University (now The University of Johannesburg), Johannesburg, South Africa, in 1992, 1994, and 1998, respectively.

He is currently the Vice President of Applications Engineering, Efficient Power Conversion Corporation, El Segundo, CA, USA. He has authored and coauthored more than 50 papers at various conferences and journals and has been granted 30 US and international patents and 26 US and international pending patent applications. He is the author and coauthor of four books. His experience covers highly resonant loosely coupled wireless power, high density dc to dc converters, GaN IC development, RF power amplifiers, solid-state high-frequency power converters and devices, utility applications of power electronics, uninterruptible power supplies, integration of power electronic converters, power electronic packaging, induction heating, photovoltaic converters, magnetic resonance imaging systems, and gate drivers with protection features.